

High Energy Collisions of Black Holes Numerically Revisited

James Healy,¹ Ian Ruchlin,^{1,2} Carlos O. Lousto,¹ and Yosef Zlochower¹

¹*Center for Computational Relativity and Gravitation,
School of Mathematical Sciences, Rochester Institute of Technology,
85 Lomb Memorial Drive, Rochester, New York 14623*

²*Department of Mathematics, West Virginia University, Morgantown, West Virginia 26506*

(Dated: October 11, 2018)

We use fully nonlinear numerical relativity techniques to study high energy head-on collision of nonspinning, equal-mass black holes to estimate the maximum gravitational radiation emitted by these systems. Our simulations include improvements in the construction of initial data, subsequent full numerical evolutions, and the computation of waveforms at infinity. The new initial data significantly reduces the spurious radiation content, allowing for initial speeds much closer to the speed of light, i.e. $v \sim 0.99c$. Using these new techniques, We estimate the maximum radiated energy from head-on collisions to be $E_{\max}/M_{\text{ADM}} = 0.13 \pm 0.01$. This value differs from the second-order perturbative (0.164) and zero-frequency-limit (0.17) analytic computations, but is close to those obtained by thermodynamic arguments (0.134) and by previous numerical estimates (0.14 ± 0.03).

PACS numbers: 04.25.dg, 04.25.Nx, 04.30.Db, 04.70.Bw

I. INTRODUCTION

The study of the high energy collision of two black holes is of interest from both the theoretical point of view, to understand gravity in its most extreme regime, and experimentally, since increasingly high energy particle collisions could eventually have a non-negligible probability for generating black hole pairs (see Ref. [1] for a review).

The production of gravitational waves and the properties of the final remnant after the collision of two black holes has been the subject of theoretical study for over half a century, with notable results such as the area theorems by Hawking and Penrose [2, 3] and their application to bounds on the energy radiated via gravitational waves. For instance, they find an upper bound for the maximum energy radiated from a head-on collision of nonspinning black holes of 29% of the total mass.

More detailed estimates of the radiated energy have been computed by applying perturbation theory [4] to the collision of ultrarelativistic black holes represented by shock waves [5]. Those computations reduce the above bound to 25% (when only including first-order corrections) and to 16.4% (when second-order corrections are included). A D -dimensional generalization of the first-order computation [6] found that the proportion of energy radiated to the initial mass scales as $1/2 - 1/D$.

Fully nonlinear numerical simulations of such collisions are now possible thanks to the breakthroughs in numerical relativity [7–9]. The first full numerical study of the head-on collision of black holes [10] found a maximum efficiency of $14 \pm 3\%$. Those studies have been extended to grazing collisions [11], leading to an estimate of 35% for the maximum energy radiated at a critical impact parameter. Further studies including boson stars [12], fluid stars [13, 14], black hole spins [15] and unequal mass binaries [16] show that, at high energies, the structure (i.e. matter, spins and mass ratios) of the holes tends to be irrelevant for the collision outcomes.

The latest analytical computations of the energy radiated by the head-on collision of two, equal mass, nonspinning black holes include an estimate of 13.4% based on black hole thermodynamics arguments [17] and 17% based on a multipolar analysis of the zero-frequency-limit (ZFL) approach [18].

In this paper we revisit the full numerical head-on computation incorporating new techniques that improve the accuracy of the simulations. These techniques include new initial data with reduced spurious radiation content [19], improved extraction techniques with second order perturbative extrapolation [20], and the use of new gauges [21] and evolution systems [22] in the moving puncture approach [8].

We use the following standard conventions throughout this paper. In all cases we use geometric units where $G = 1$ and $c = 1$. Latin letters (i, j, \dots) represent spatial indices. Spatial 3-metrics are denoted by γ_{ij} and extrinsic curvatures by K_{ij} . The trace-free part of the extrinsic curvature is denoted by A_{ij} . A tilde indicates a conformally related quantity. Thus $\gamma_{ij} = \psi^4 \tilde{\gamma}_{ij}$ and $A_{ij} = \psi^{-2} \tilde{A}_{ij}$, where ψ is some conformal factor. We denote the covariant derivative associated with γ_{ij} by D_i and the covariant derivative associated with $\tilde{\gamma}_{ij}$ by \tilde{D}_i . A lapse function is denoted by α , while a shift vector by β^i .

II. NUMERICAL TECHNIQUES

A. Initial Data

We use an extended version TWOPUNCTURES [23] thorn to generate puncture initial data [19] for boosted black hole binary simulations. In the conformal transverse-traceless (CTT) formalism [24–27], the constraints on the initial spatial hypersurface Σ_0 become a

set of elliptic differential equations for the conformal factor and potential vector (see Eq. (11) below) through a conformal transformation

$$\gamma_{ij} = \psi^4 \tilde{\gamma}_{ij} .$$

We call $\tilde{\gamma}_{ij}$ the conformally related metric tensor. All objects with a tilde are associated with $\tilde{\gamma}_{ij}$.

As in Ref. [19], to calculate the spatial metric and extrinsic curvature associated with a boosted black hole of mass m and arbitrary linear 3-momentum P^i , we Lorentz boost the 4-dimensional Schwarzschild line element in isotropic Cartesian coordinates. We then extract from the transformed metric the spatial metric γ_{ij}^* , the lapse function α^* , and the shift vector β_i^* (a super/subscript $*$ indicates that this is a single black hole quantity). We then obtain the extrinsic curvature K_{ij}^* on Σ_0 using the evolution equation for the spatial metric

$$K_{ij}^* = \frac{1}{2\alpha^*} (D_i^* \beta_j^* + D_j^* \beta_i^* - \partial_t \gamma_{ij}^*) .$$

CTT separates this into trace and trace-free parts

$$K_{ij}^* = \psi_*^{-2} \tilde{A}_{ij}^* + \frac{1}{3} \psi_*^4 \tilde{\gamma}_{ij}^* K^* ,$$

where $K^* = \gamma_*^{ij} K_{ij}^*$. For the conformal factor, we make the standard choice

$$\psi^* = 1 + \frac{m}{2r} , \quad (1)$$

where r is the unboosted isotropic radius.

For example, if the boosted coordinates are given by

$$t' = \gamma t + \gamma v y , \quad (2)$$

$$x' = x , \quad (3)$$

$$y' = \gamma y + \gamma v t , \quad (4)$$

$$z' = z , \quad (5)$$

then the conformal spatial line element on Σ_0 (defined by $t' = \text{const}$) is given by

$$d\tilde{\ell}^2 = dx'^2 + \gamma^2 \left[1 - \frac{16(m-2r)^2 r^4 v^2}{(m+2r)^6} \right] dy'^2 + dz'^2 , \quad (6)$$

where v is the magnitude of the local velocity vector

$$v^i = \frac{P^i}{\sqrt{m^2 + P^j P_j}} \quad (7)$$

(here the boost is along the y -axis), $\gamma = (1 - v^2)^{-1/2}$, and $r = \sqrt{x^2 + y^2 + z^2} = \sqrt{x'^2 + \gamma^2(y' - vt')^2 + z'^2}$.

Our black hole binary initial data is constructed using a superposition of metric and extrinsic curvature terms derived from the above expressions. To distinguish contributions for the two black holes, we replace the $*$ super/subscript above with a $+$ or $-$.

The trace-free part of the extrinsic curvature is split into background terms \tilde{M}_{ij} and a longitudinal correction term obtained from a vector b_i . Here

$$\tilde{M}_{ij} = \tilde{A}_{ij}^{(+)} + \tilde{A}_{ij}^{(-)} , \quad (8)$$

where $\tilde{A}_{ij}^{(+)}$ and $\tilde{A}_{ij}^{(-)}$ are the trace-free part of the conformal extrinsic curvature of a single boosted black holes located at $\vec{r} = \vec{r}_+$ and $\vec{r} = \vec{r}_-$. Note that the trace-free part of the single boosted black hole extrinsic curvature will have a small trace with respect to a metric constructed by superimposing two different background metrics. We remove this extra trace term prior to solving the initial data equations, i.e., $\tilde{M}_{ij} \rightarrow \tilde{M}_{ij} - \frac{1}{3} \tilde{\gamma}_{ij} \tilde{\gamma}^{lm} \tilde{M}_{lm}$ (where $\tilde{\gamma}_{ij}$ is the superimposed background metric). The complete trace-free part of the extrinsic curvature for the superimposed spacetime is given by

$$\tilde{A}_{ij} = \tilde{M}_{ij} + \frac{1}{\alpha} (\tilde{\mathbb{L}}b)_{ij} , \quad (9)$$

where $\alpha = \psi^6 \tilde{\alpha}$ and $(\tilde{\mathbb{L}}b)_{ij} \equiv \tilde{D}_i b_j + \tilde{D}_j b_i - \frac{2}{3} \tilde{\gamma}_{ij} \tilde{D}_k b^k$ is the longitudinal vector gradient. As part of the freely specifiable parameters we set $\tilde{\alpha} = 1$.

In the puncture approach, we write the conformal factor as singular parts plus a finite correction, u ,

$$\psi = \psi_{(+)} + \psi_{(-)} - 1 + u , \quad (10)$$

where $\psi_{(\pm)}$ are the conformal factors (1) associated with the individual, isolated black holes located at positions labeled as $(+)$ and $(-)$, with spatial metric tensors $\tilde{\gamma}_{ij}^{(\pm)}$.

Given these choices, the Hamiltonian and momentum constraints become equations for the correction functions u and b^i

$$\tilde{D}^2 u - \frac{\psi \tilde{R}}{8} - \frac{\psi^5 K^2}{12} + \frac{\tilde{A}_{ij} \tilde{A}^{ij}}{8\psi^7} + \tilde{D}^2 (\psi_{(+)} + \psi_{(-)}) = 0 , \quad (11a)$$

$$\tilde{\Delta}_{\mathbb{L}} b^i + \tilde{D}_j \tilde{M}^{ij} - \frac{2}{3} \psi^6 \tilde{\gamma}^{ij} \tilde{D}_j K = 0 , \quad (11b)$$

where $\tilde{\Delta}_{\mathbb{L}} b^i \equiv \tilde{D}_j (\tilde{\mathbb{L}}b)^{ij}$ is the vector Laplacian and \tilde{R} is the scalar curvature associated with $\tilde{\gamma}_{ij}$. The solutions are required to obey Dirichlet conditions at infinity

$$\lim_{r \rightarrow \infty} u = 0 \quad \text{and} \quad \lim_{r \rightarrow \infty} b^i = 0 .$$

In order to deal with the puncture singularities, we introduce attenuation functions to both modify the background metric and mean curvature, as well as modify the singular source terms inside the horizons themselves. The first type of attenuation, which is consistent with the constraints everywhere, is used in the superposition of the background conformal metrics and has the form,

$$\tilde{\gamma}_{ij} = \delta_{ij} + f_{(+)} \left(\tilde{\gamma}_{ij}^{(+)} - \delta_{ij} \right) + f_{(-)} \left(\tilde{\gamma}_{ij}^{(-)} - \delta_{ij} \right) ,$$

where

$$f_{(\pm)} = 1 - e^{-(r_{(\mp)})/\omega_{(\pm)}}^p,$$

and $r_{(\pm)}$ is the coordinate distance from a field point to the location of puncture (\pm) . The parameters $\omega_{(\pm)}$ control the steepness of the attenuation. We take the smallest possible power index $p = 4$ to achieve convergence of the solutions to the constraints.

The second attenuation function is used to modify the background mean curvature and the source term in the momentum constraint equations. This takes the form

$$\begin{aligned} K &= f_{(+)}gK_{(+)} + f_{(-)}gK_{(-)}, \\ \tilde{D}_i\tilde{M}^{ij} &= g\tilde{D}_i\tilde{A}_{(+)}^{ij} + g\tilde{D}_i\tilde{A}_{(-)}^{ij}, \end{aligned}$$

where

$$\begin{aligned} g &= g_+ \times g_-, \\ g_{\pm} &= \begin{cases} 1 & \text{if } r_{\pm} > r_{\max} \\ 0 & \text{if } r_{\pm} < r_{\min} \\ \mathcal{G}(r_{\pm}) & \text{otherwise,} \end{cases} \\ \mathcal{G}(r_{\pm}) &= \frac{1}{2} \left[1 + \tanh \left(\tan \left[\frac{\pi}{2} \left(-1 + 2 \frac{r_{\pm} - r_{\min}}{r_{\max} - r_{\min}} \right) \right] \right) \right], \end{aligned}$$

and the parameters $r_{\min} < r_{\max}$ are chosen to be within the horizon. Note that the g attenuation function is used to modify the constraint equations themselves inside the horizon. We will refer to the above data as the *standard data* in the sections below.

In addition, we consider a second type of initial data closely related to the above approach. For this, which we shall refer to as *approximate data* in the sections below, we analytically remove the singularity associated with $\tilde{D}_i\tilde{M}^{ij}$ by making the following two approximations. First, we take \tilde{M}_{ij} to be the sum of the two Kerr trace-free extrinsic curvatures without correcting for the fact that the background metric is now a superimposed metric. Second, in the source term of Eq. (11b), we replace $\tilde{D}_i\tilde{A}_{\pm}^{ij}$ with $(\tilde{D}_i - \tilde{D}_i^{\pm})\tilde{A}_{\pm}^{ij} + \tilde{D}_i^{\pm}\tilde{A}_{\pm}^{ij}$, where \tilde{D}_i^{\pm} and \tilde{A}_{\pm}^{ij} are the covariant derivative and extrinsic curvature associated with the two background conformal Kerr metrics. The former term contains no derivatives of \tilde{A}_{\pm}^{ij} , while the latter is evaluated analytically. This is an additional approximation because we neglect the fact that indices in \tilde{A}_{\pm}^{ij} are actually raised using the full superposed metric, rather than the associated Kerr metric. The net result of these approximations is that the initial data solution converges (relatively) rapidly with collocation points, but the resulting constraints converge to a small non-zero value. We use a subsequent CCZ4 evolution to remove this residual violation. This allow us to quantify the effects of small violations of the initial constraints and how to control them.

B. Convergence of Initial Data

As shown in Fig. 1, we verified the exponential convergence of the constraint violations of the initial data (with collocation points) using the L^2 -norms (RMS). We find that volume-averaged constraint violation (i.e., L^2 over the entire simulations domain) converge to levels of $\sim 5 \times 10^{-10}$. The constraint violations are largest near the x -axis (see Fig. 2). To verify the convergence of the data there, we calculated the L^2 -norm over as small box of width $0.5M$ centered on the x -axis. This box is chosen so that it lies just outside one of the horizons. The momentum constraints converge exponentially, but at a relatively slow rate, in this volume. The Hamiltonian converges exponentially to a level of $\sim 10^{-7}$. The source of the relatively large violations is a high-frequency component in the initial data induced by the scale of the attenuation function. Note that the convergence of the *approximate data* is much faster with collocation points, but also converges to a non-zero value.

Figure 2 shows the initial data Hamiltonian constraint violation on the xy -plane for a configuration with $P/m_{\text{irr}} = 1$ and initial separation $d/M = 10$. Note the high-frequency residual. By increasing the width of the attenuation function g above, we were able to partially mitigate the high-frequency noise in the constraint residuals using $N = 192^2 \times 4$ collocation points. For comparison we also show the same configuration with $P/m_{\text{irr}} = 1$ and initial separation $d/M = 10$ but for $N = 48^2 \times 4$ collocation points, which represents a medium resolution for BY data. The choice of a lower number of collocation points ($N = 48^2 \times 4$) for BY is because the BY system is algebraically simpler than the new data (among others, the momentum constraints are solved exactly, and the background is flat). We thus expect that for a given number of collocation points, BY data will have a much smaller constraint violation, which is indeed what we see (see bottom panels of this figure). From the figure, we see that we can reach acceptable levels of constraint violations with our data, but require a much larger number of collocation points than for BY.

C. Evolution

We evolve black hole binary initial data sets using the LAZEV [28] implementation of the moving punctures approach for both the BSSNOK formalism [29–31] and the conformal and covariant formulation of the Z4 (CCZ4) system (Ref. [22]) which includes stronger damping of the constraint violations than the BSSNOK system. For the runs presented here, we use centered, eighth-order accurate finite differencing in space [32] and a fourth-order Runge-Kutta time integrator. Our code uses the CACTUS/EINSTEINTOOLKIT [33, 34] infrastructure. We use the CARPET mesh refinement driver to provide a “moving boxes” style of mesh refinement [35]. Fifth order Kreiss-Oliger dissipation is added to evolved variables with dis-

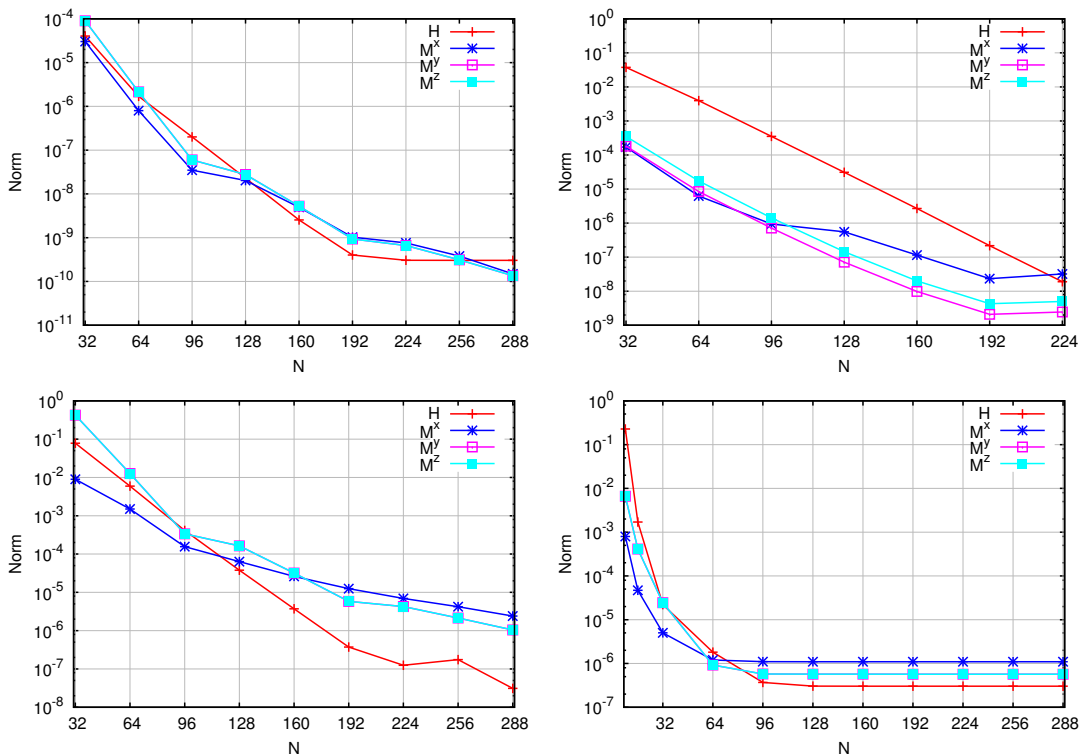


FIG. 1. The L^2 -norms of the Hamiltonian and momentum constraints for the *standard data* over the full grid extending to $400M$ (top-left), over a small volume centered on $(x, y, z) = (5.0, 0.35, 0.75)$ (top-right), over a small volume containing the x -axis centered on $(4.5, 0, 0)$ (bottom-left). The number of collocation points is given by $N \times N \times 32$ in the A , B , and ϕ dimensions, respectively. The bottom-right plot shows the constraint violation over the full grid with the *approximate data* instead.

sipation coefficient $\epsilon = 0.1$. Note that when using CCZ4, we chose damping parameters $\kappa_1 = 0.1$, $\kappa_2 = 0$, and $\kappa_3 = 0$ (see [22]).

We locate the apparent horizons using the AHFINDERDIRECT code [36] and measure the horizon spins using the isolated horizon (IH) algorithm [37]. To compute the radiated angular momentum components, we use formulas based on “flux-linkages” [38], explicitly written in terms of Ψ_4 [39, 40]. We then extrapolate those extractions to an infinite observer location using formulae accurate to $\mathcal{O}(1/r_{\text{obs}}^2)$ [20].

We obtain accurate, convergent waveforms and horizon parameters by evolving this system in conjunction with a modified 1+log lapse and a modified Gamma-driver shift condition [8, 41, 42]. The lapse and shift are evolved with

$$(\partial_t - \beta^i \partial_i) \alpha = -\alpha^2 f(\alpha) K, \quad (12a)$$

$$\partial_t \beta^a = \frac{3}{4} \tilde{\Gamma}^a - \eta \beta^a. \quad (12b)$$

where $\eta = 2$.

We have found that the choice $f(\alpha) = 8/(3\alpha(3 - \alpha))$ (approximate shock avoiding [21]) proves to be more stable and convenient when dealing with highly boosted moving punctures at relatively short separations, $\approx 100M$ (this proved particularly useful for the CCZ4

simulations described below). This is due to the fact that the shock avoiding gauge suppresses a large amplitude gauge wave that would otherwise be focused by the black holes and subsequently trigger a Courant violation when the lapse gets too big. For the initial form of the lapse we use $\alpha(t = 0) = 1/(2\psi_{\text{BL}} - 1)$, where $\psi_{\text{BL}} = 1 + m_{(+)/(2r_{(+)})} + m_{(-)/(2r_{(-)})}$. This proved to produce more accurate evolutions for highly spinning black holes [19] and we will also adopt it for the highly boosted cases in this paper.

For both sets of evolutions, CCZ4 and BSSNOK, there are between 11 and 13 levels of mesh refinement depending on the momentum of the black holes. Since we start the initial separations of the CCZ4 simulations much farther apart than the BSSNOK evolutions, the coarsest levels of the grid structure differ between the two sets of evolution. The CCZ4 evolutions have an outer boundary of $800M$, while the BSSNOK evolutions have an outer boundary of $400M$. The finest levels are the same for both sets of evolutions. We label the different resolution runs by nX where X is a global grid factor. For all evolution runs, we use a grid of $n120$. For this case, the finest resolution for the $P/m_{\text{irr}} = 0.3$ case is $M/307.2$ and finest resolution for the $P/m_{\text{irr}} = 4.0$ case is $M/1228.8$. Full details of the $n120$ grid structure is given in Table I.

Figure 3 shows the constraint violations versus time

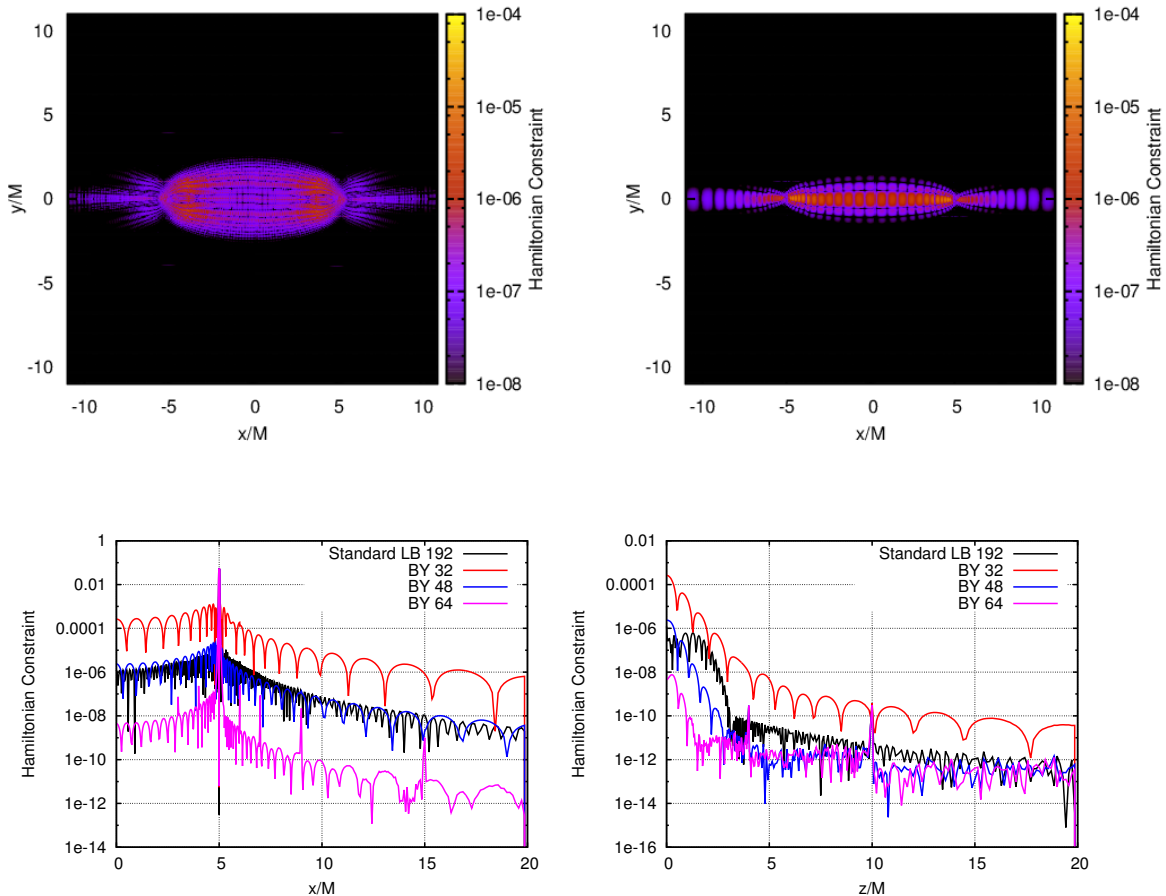


FIG. 2. The Hamiltonian constraint in the xy -plane of the *standard data* for $P/m_{\text{irr}} = 1$ with initial separation $d/M = 10$ in the region around the black holes for $N = 192$ collocation points (Top left). For comparison we also show the violations of the Hamiltonian constraint for BY data for $N = 48$ collocation points (Top right). In the lower panels we show the violation of the Hamiltonian constraint along the axis containing the black holes and perpendicular to it for our data and for BY data for different number of collocation points $N = 32, 48, 64$.

for a $P/m_{\text{irr}} = 2$ simulation using BSSNOK evolutions of *standard data* for three resolutions ($n100$, $n120$, $n144$). During most of the run, after the initial settling of gauges, the constraint violations are convergent. We observe a hyperconvergent (4th-8th) order for the merger phase and then a slower convergence (due to residual grid interboundary radiation) of nearly first order after merger.

III. RELATIVISTIC HEAD-ON COLLISIONS

A major difference between our work here and previous studies, see Refs. [10, 11, 15, 16], is that we use non-conformally flat initial data. The Bowen-York initial data used previously are limited to representing black holes moving at speeds $v < 0.9c$, as shown in Fig. 4. The reason for this is that the assumption of conformal flatness introduces a Brill wave that gets stronger as the momentum parameter is increased. Most of this wave is

absorbed by the black holes, leading them to increase in mass proportional to the momentum parameter. The net effect is that the ratio of momentum to mass of each black hole can never be larger than $P/m_{\text{irr}} \sim 2$ (i.e., $v/c \sim 0.9$). Note that here we use the irreducible mass of each black hole in place of the particle rest mass.

The situation is similar to that observed in highly spinning black holes, where the conformally flat ansatz for the 3-metric leads to a limitation [43–45] in the maximum intrinsic spin of the black hole of around $S/m^2 \approx 0.93$.

On the other hand, Fig. 4 shows that the new data we use here is not limited by this condition and can reach velocities closer to the speed of light, i.e. $v \sim 0.99c$. This is due to the much lower initial radiation content of the data. We will exploit this characteristic of the initial data to obtain a more accurate estimate of the maximum gravitational radiation produced by head-on collision of two equal mass, nonspinning, black holes.

In order to explore the dependence of the radiated en-

TABLE I. Table of grid structure for case $n120$. For P/m_{irr} up to 2 we use up to mesh level 10. For $P/m_{\text{irr}} = 3$ we include an additional level and for $P/m_{\text{irr}} = 4$ we use all 13 mesh refinement levels. Whether the refinement level's grid is centered on the origin or around the black holes (BHs) is given in column 2. The radius of the box is given in column 3. For meshes with two values, the first is for the BSSNOK evolution of the *standard data*, and the second is for the CCZ4 evolutions of the *approximate data*.

Mesh Number	Centered on	Radius	Resolution
0	Origin	400,800	$M/0.3$
1	Origin	200,500	$M/0.6$
2	Origin	140,300	$M/1.2$
3	BHs	32	$M/2.4$
4	BHs	16	$M/4.8$
5	BHs	8	$M/9.6$
6	BHs	4	$M/19.2$
7	BHs	2	$M/38.4$
8	BHs	1.2	$M/76.8$
9	BHs	0.6	$M/153.6$
10	BHs	0.3	$M/307.2$
11	BHs	0.15	$M/614.4$
12	BHs	0.08	$M/1228.8$

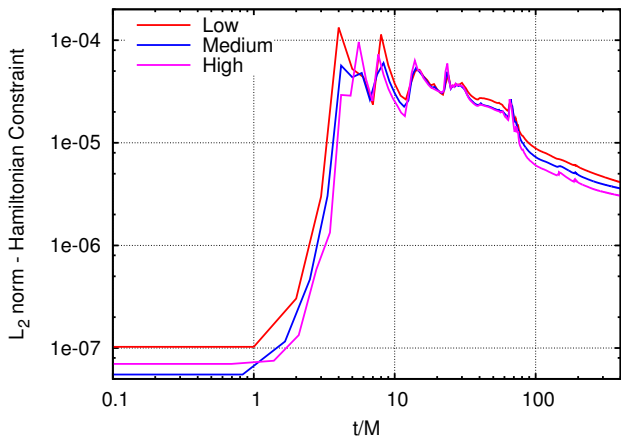


FIG. 3. The L^2 -norm of the Hamiltonian constraint violation versus time for a $P/m_{\text{irr}} = 2$ simulations using *standard data* evolved with BSSNOK at three different resolutions. At early times, the constraint violations are much smaller, but the violations become much larger than their initial values for most of the simulation. Globally the constraints decrease with resolution only slightly due to high-frequency noise on the grid.

ergy on the magnitude of initial momentum of the two black holes, and then extrapolate the results to the ultrarelativistic limit, we set up a series of simulations with P/m_{irr} ranging from 0.3 to 4.03 (see Tables II and III). We have chosen a relatively large initial separation of the black holes in order to ensure that the isolated horizon formalism can be used to accurately measure the mass of the black holes and to ensure that the momentum parameter used in the simulations corresponds closely to

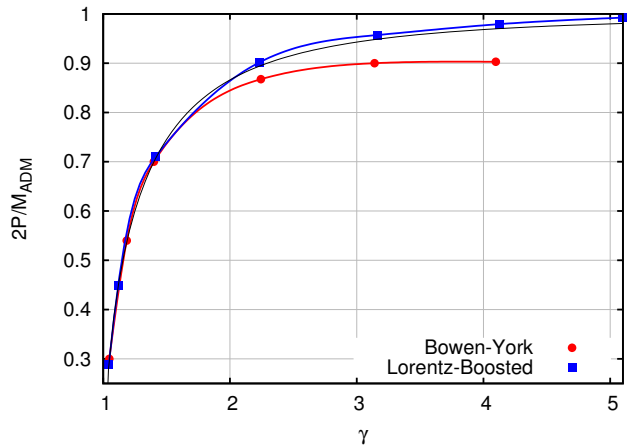


FIG. 4. The center of mass speeds of the black holes for the Lorentz boosted data in this paper and Bowen-York data. The latter displays a limitation, reaching speeds of only $v < 0.9c$, while the former can reach near the ultrarelativistic regime. The thin line represent the special relativistic speed expression $v = c\sqrt{1 - 1/\gamma^2}$.

the momentum of the black holes at infinite separation.

In Fig. 5, we show the $(\ell = 2, m = 2)$ mode of ψ_4 for a typical simulations (here $P/m_{\text{irr}} = 2$) as seen by an observer at $r = 130M$. The spurious radiation is evident in the burst near $t \sim 150M$, well before the merger signal. As can be seen from the figure, for the new data, the spurious radiation contains about 4% of the total energy radiated for the *standard data*. On the other hand, the Bowen-York spurious radiation content is 24% of the total.

To extrapolate the energy radiated to infinite observer location, we use 7 finite observers and extrapolate using a 1st order and 2nd order polynomial.

For the *standard data* simulations (which were all evolved using BSSNOK), the extraction radii extended to $r_{\text{obs}} = 130M$. The error in the extrapolation is estimated by the difference between the two fits and is labeled “Inf Radius” error in Fig. 6.

For the simulations of the *approximate data* (which were all evolved using CCZ4), we needed to use larger initial separations than for the *standard data* in order to reduce the constraint violations on the initial slice. We therefore extracted the radiation at correspondingly large distances. For example, for the largest separation run $d = 400M$, the largest extraction radius as $275M$ (note the black holes were initially located at $x = \pm 200M$).

In all of the CCZ4 cases, the extrapolation formula of Ref. [20] to $\mathcal{O}(1/r_{\text{obs}}^2)$ gives a very robust set of values for the radiated energy. To provide a generous bound, we used those two radii as estimates of the infinite radius energy radiated.

The other source of error we seek to keep under control is the initial, unphysical radiation content. We checked this spurious radiation for all of the Lorentz boosted runs. To do this, we compare the radiated energy of the

TABLE II. Table of initial parameters and energy radiated for the *standard initial data* evolved with BSSNOK.

P/M_{ADM}	M_{ADM}/M	$m_{\text{irr}}/M_{\text{ADM}}$	P/m_{irr}	γ	d/M	$E_{\text{rad}}/M_{\text{ADM}}$	$\delta E_{\text{rad}}/M_{\text{ADM}}$
0.1437	1.0008	0.4804	0.30	1.0438	100	0.0011	4.8e-5
0.2238	1.0028	0.4488	0.50	1.1174	100	0.0031	1.3e-6
0.3547	1.0093	0.3555	1.00	1.4126	100	0.0182	2.6e-4
0.4510	1.0177	0.2583	2.00	2.2336	100	0.0585	1.3e-3
0.4792	1.0268	0.1597	3.00	3.1630	100	0.0858	1.8e-3
0.4886	1.0250	0.1220	4.00	4.1272	150	0.0957	1.3e-4

TABLE III. Table of initial parameters and energy radiated for the *approximate data* evolved with CCZ4. For each system, the initial ADM mass is normalized to 1.

P/M_{ADM}	M_{ADM}/M	$m_{\text{irr}}/M_{\text{ADM}}$	P/m_{irr}	γ	d/M_{ADM}	$E_{\text{rad}}/M_{\text{ADM}}$	$\delta E_{\text{rad}}/M_{\text{ADM}}$
0.1439	1.0000	0.4807	0.30	1.0440	100	0.0011	6.8e-7
0.2245	1.0000	0.4498	0.50	1.1180	100	0.0030	6.1e-6
0.3558	1.0000	0.3559	1.00	1.4142	200	0.0183	1.2e-4
0.4530	1.0000	0.2263	2.00	2.2361	200	0.0592	4.7e-4
0.4800	1.0000	0.1594	3.01	3.1717	300	0.0859	1.1e-3
0.4908	1.0000	0.1217	4.03	4.1231	400	0.0988	9.7e-4

full waveform with that obtained by removing the initial transient. The effect of the initial transient is to change the total radiated energy by $\sim 1.6\%$ (relative to the total radiated energy). The effect of this spurious radiation on the accuracy of the total radiated energy is shown in Fig. 6 under the label “Spurious”.

It is worth noting here that the waveforms are extracted by a multipole decomposition at the observer location. In practice a few of the lower modes are necessary for an accurate account of the total radiation. For instance, the ℓ -mode contributions to the CCZ4 simulations for a $P/m_{\text{irr}} = 3$ run (with initial separation $d = 100M$) at $r_{\text{obs}} = 275M$ gives that $\ell = 2$ contains 90%, $\ell = 4$ contains 8.3%, and $\ell = 6$ contains 1.68% of the total energy radiated. Thus our results will include modes up to $\ell = 6$.

To test the accuracy and consistency of our simulations, we performed a convergence study of the radiated energy, the main physical quantity studied here, for six runs (all with initial $P/m_{\text{irr}} = 0.5$). We increase the resolution in stepsizes of 1.2 between each run. The results of evaluation of the final mass of the black hole from the measurement of the gravitational radiation losses is shown in Fig. 7. While the differences with resolution are small, they are compatible with the expected 4th order convergence of the evolution system. In this figure, we fit the data to the form $y = a_0 + a_1 x^p$, where a_0 and a_1 are fitting constants and p is taken to be 2, 4, and 6.

Also for runs with initial $P/m_{\text{irr}} = 2$, the agreement between the radiated energies, as measured from the waveforms (extrapolated to observer location to infinity via [20]) and those inferred from the initial ADM mass minus the remnant horizon mass, provides a consistency measure for the numerical simulation (here we increased the resolution by factors of 1.1). Assuming the differences scales like $a h^b$, the b -power of convergence for the three highest resolution h runs is found to be 4.17697 ± 1.139 .

In addition, we fit the same data to the form $a h^b + c$, where b was fixed to 1, 2, 3, 4, and 5, and for each choice of b , we fit to a and c . The results are summarized in Fig. 8, which shows different orders of extrapolation to infinite resolution. The best results are near the expected 4th order convergence. Here, we find consistency in the final mass to within $5 \times 10^{-5}M$.

Another interesting aspect to explore is how appropriate the standard moving puncture gauges (12) are for evolving highly-boosted black holes. We found that at relatively short initial distances the BSSNOK formalism generates a gauge wave focused by the two black holes that then induces a large change in the lapse. This can drive the lapse beyond $\alpha = 1$ and trigger a Courant violation. This problem was resolved by starting the black holes at larger initial separations, allowing the large gauge waves to sufficiently dissipate before the collision. We also found it beneficial to use an initial lapse of the form $\alpha_0 = 1/(2\psi_{\text{BL}} - 1)$ and the approximate shock avoiding gauge profile $f(\alpha) = 8/(3\alpha(3 - \alpha))$ (which we used for all CCZ4 simulations).

When fitting the radiated energy as a function of the initial momentum we assume a relative error of 1% in each computed energy to determine its weight in the fit. We fit these energy values as a function of the variable m_{irr}/P , where m_{irr} stands for the irreducible mass of each initially boosted black hole with momentum $\pm P$. The upper panels in Fig. 9 and 10 display the results of the fitting, assuming the dependence of the energy radiated is given by the ZFL behavior [10, 46]

$$\frac{E}{M} = E_{\infty} \left(\frac{1 + 2\gamma^2}{2\gamma^2} + \frac{(1 - 4\gamma^2) \log(\gamma + \sqrt{\gamma^2 - 1})}{2\gamma^3 \sqrt{\gamma^2 - 1}} \right), \quad (13)$$

where $\gamma = \sqrt{1 + (P/m_{\text{irr}})^2}$ and the only fitting parameter is E_{∞} . The relative deviations are mostly below 10%, and in particular are around 2% for the most energetic

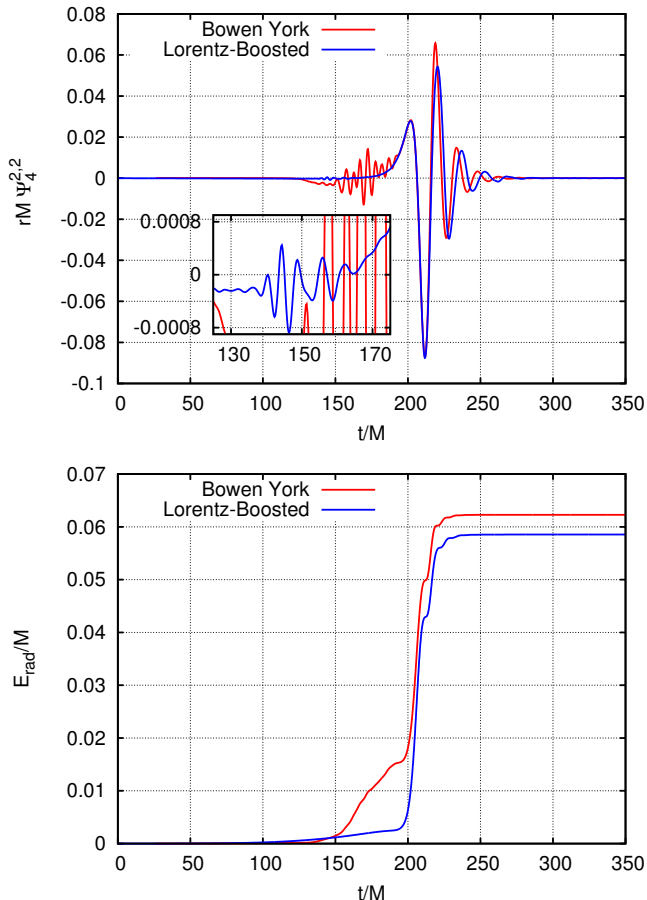


FIG. 5. Top panel: The $(\ell = 2, m = 2)$ mode of ψ_4 for the $P/m_{\text{irr}} = 2$ Bowen-York and Lorentz-Boosted simulations. Note the spurious signal at $t \sim 150M$. The inset zooms in on the spurious signal of the Lorentz-Boosted waveform. Bottom Panel: The energy radiated for the two waveforms in the top panel. The contribution of the spurious radiation can be seen by looking at the energy radiated up to time $t \sim 200M$.

simulated collision.

To assess the dependence with the chosen fitting function, we have assumed a fit of the form ($y = A \exp[-Bx]$) with two fitting parameters (A and B), y and x being the independent and dependent variables, i.e. $E_{\text{rad}}/M_{\text{ADM}}$ and m_{irr}/P , respectively. The results of this fit are displayed in the lower panels of Fig. 9 and 10. In spite of introducing two fitting parameters, we observe that the residuals are larger than the fit using the ZFL form (13), thus rendering further support to this behavior. We have also experimented with fittings of the form ($y = A \exp[-Bx^C]$), introducing a third parameter C in the fitting function, and also assuming $C = 2$, but none of these options displayed better behavior than the ZFL choice.

In either case of the fits shown in Fig. 10, the estimated maximum radiated energy is around 13%, which provides a robust estimate, all errors considered, of the form $E_{\text{max}}/M_{\text{ADM}} = 0.13 \pm 0.01$.

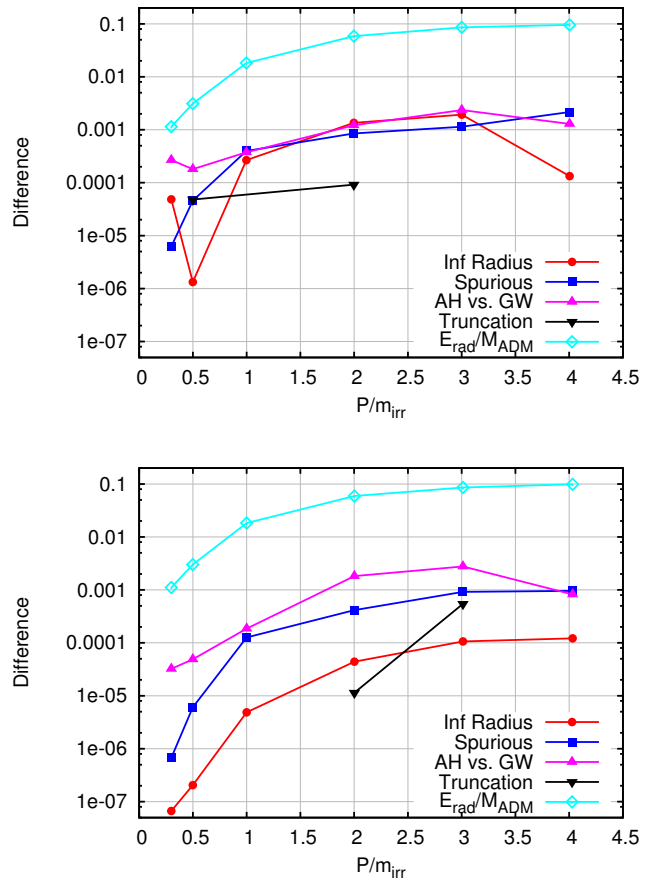


FIG. 6. Estimated errors for each component of the computation of the radiated energy. “Inf Radius” is the extrapolation from the finite extraction radius r_{obs} to infinity. “Spurious” is the effect of the initial radiation content of the data. “Truncation” is an estimate of the finite difference resolution used in the simulation, and “AH vs. GW” is a consistency measure of the radiated energy as computed by the gravitational waveforms or the remnant mass of the final black hole. Shown in cyan is the total energy radiated for that simulation. Top panel is the BSSNOK evolutions of the *standard data*, and bottom panel is for the CCZ4 evolutions of the *approximate data*.

IV. CONCLUSIONS AND DISCUSSION

Using improved full numerical techniques, we have been able to provide a more accurate determination of the maximum gravitational radiation produced in the head-on collision of nonspinning black holes. These techniques utilize initial data for highly boosted black holes [19] with much less radiation content than the Bowen-York counterparts, and reach near the ultrarelativistic regime with speeds much closer to c . We have successfully extrapolated the extracted waveforms to infinite observer locations with the techniques of Ref. [20], and added up to $\ell = 6$ modes in the computation of the radiated energy. The evolutions of the initial data have been carried

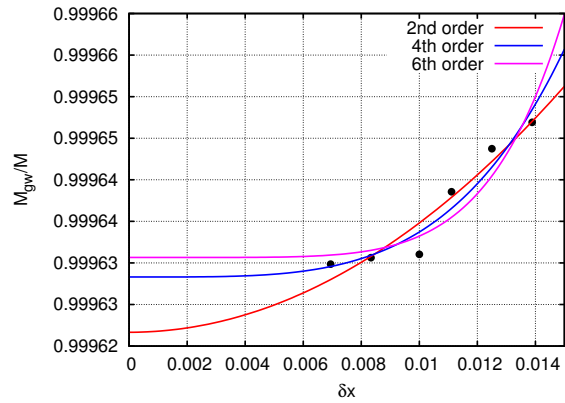


FIG. 7. The convergence for the $P/m_{\text{irr}} = 0.50$ final mass calculated from the gravitational modes ($\ell_{\text{max}} = 6$). sixth-, fourth-, and second-order fits to the data are shown. The fourth-order fit is closest to the data. For this convergence study, we used six runs ($n72, n80, n90, n100, n120, n144$).

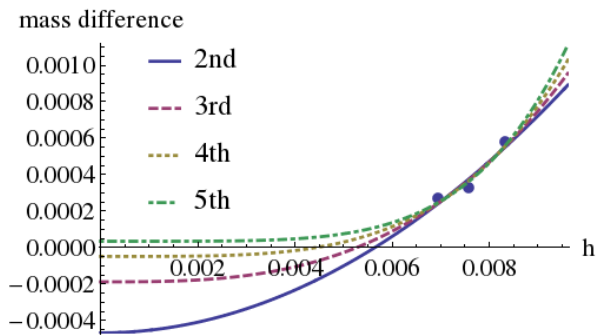


FIG. 8. The difference between the final horizon mass as calculated using the IH formalism and as inferred from the radiated energy for a $P/m_{\text{irr}} = 2$ simulation as a function of resolution. The three highest resolution runs are shown. The data points themselves appear to be convergent. We estimate the infinite resolution limit by assuming second, third, fourth-order, and fifth-order convergence. The agreement between the horizon derived mass and radiation inferred mass at infinite resolution is $5 \times 10^{-5}M$ for the expected 4th order convergence.

out using the moving punctures approach using both the BSSNOK and CCZ4 systems.

We find a maximum radiated energy of $13 \pm 1\%$ of the total mass of the system, with most of the errors coming from the functional fitting and subsequent extrapolation to infinite boost. This result is in close agreement with the analytic estimates of 13.4% of Ref. [17] using thermodynamic arguments and the previous numerical estimate of $14 \pm 3\%$ in Ref. [11]. However, they seem to be in conflict with the analytic estimates of 16.4% from second order perturbations [4] and 17% from the

multipolar analysis of the ZFL [18].

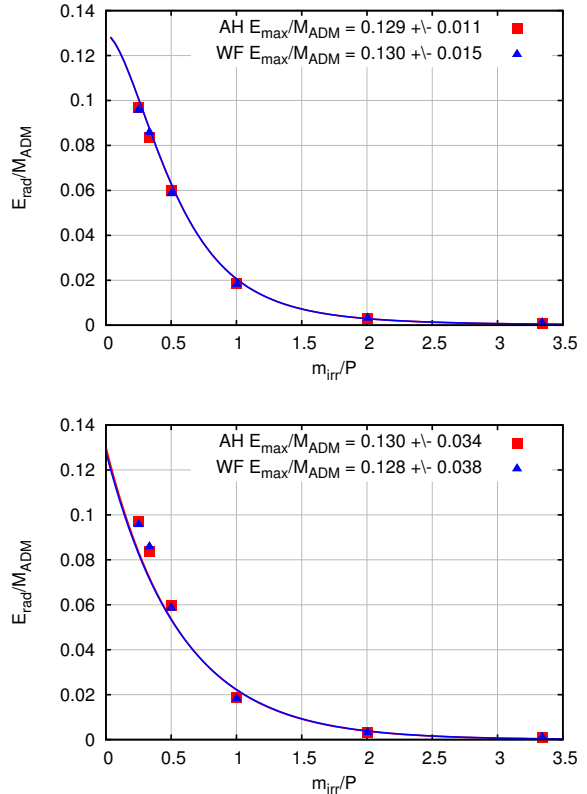


FIG. 9. Fits to the energy radiated at infinity for the BSSNOK evolutions of the *standard data* in Table II. Upper plot: Fit using the 1-parameter ZFL like fit. Lower plot: An alternative two-parameter (A and B) fit of the form ($y = A \exp[-Bx]$). Both fits use data assuming a weighting error of the points of 1% and include fits to both the energy radiated as measured by extraction of radiation (WF) or by the remnant mass (AH).

ACKNOWLEDGMENTS

The authors thank M. Campanelli for helpful discussions. The authors gratefully acknowledge the NSF for financial support from Grants PHY-1305730, PHY-1212426, PHY-1229173, AST-1028087, PHY-0969855, OCI-0832606, and DRL-1136221. Computational resources were provided by XSEDE allocation TG-PHY060027N, and by NewHorizons and BlueSky Clusters at Rochester Institute of Technology, which were supported by NSF grant No. PHY-0722703, DMS-0820923, AST-1028087, and PHY-1229173. This work was supported in part by the 2013–2014 Astrophysical Sciences and Technology Graduate Student Fellowship, funded in part by the New York Space Grant Consortium, administered by Cornell University.

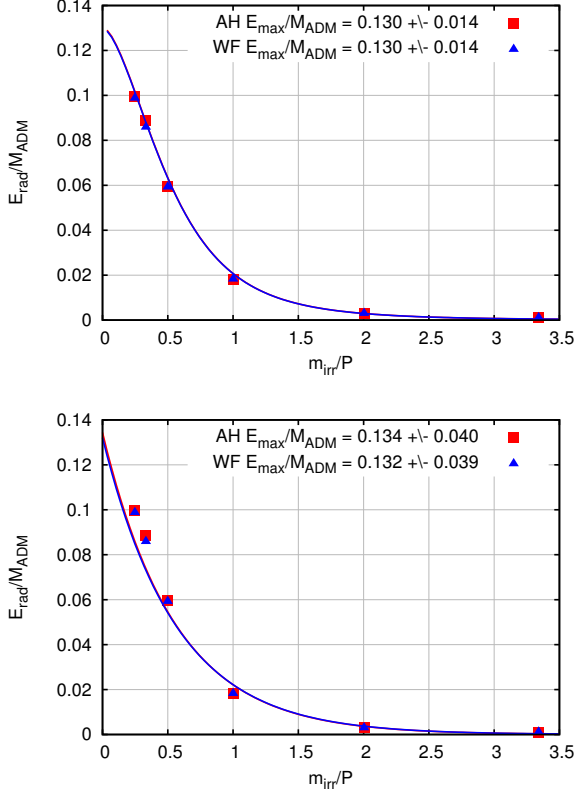


FIG. 10. Fits to the energy radiated at infinity for the CCZ4 evolutions of the *approximate data* in Table III. Upper plot: Fit using the 1-parameter ZFL like fit. Lower plot: An alternative two-parameter (A and B) fit of the form ($y = A \exp[-B x]$). Both fits use data assuming a weighting error of the points of 1% and include fits to both the energy radiated as measured by extraction of radiation (WF) or by the remnant mass (AH).

-
- [1] V. Cardoso, L. Gualtieri, C. Herdeiro, U. Sperhake, P. M. Chesler, L. Lehner, S. C. Park, H. S. Reall, C. F. S. (section coordinators), D. Alic, O. J. C. Dias, R. Emparan, V. Ferrari, S. B. Giddings, M. Godazgar, R. Gregory, V. E. Hubeny, A. Ishibashi, G. Landsberg, C. O. Lousto, D. Mateos, V. Moeller, H. Okawa, P. Pani, M. A. Parker, F. Pretorius, M. Shibata, H. Sotani, T. Wiseman, H. Witek, N. Yunes, and M. Zilhão, *Class. Quant. Grav.* **29**, 244001 (2012), arXiv:1201.5118 [hep-th].
- [2] S. Hawking, *Phys. Rev. Lett.* **26**, 1344 (1971).
- [3] D. M. Eardley and S. B. Giddings, *Phys. Rev.* **D66**, 044011 (2002), arXiv:gr-qc/0201034 [gr-qc].
- [4] P. D'Eath and P. Payne, *Phys. Rev.* **D46**, 694 (1992).
- [5] P. Aichelburg and R. Sexl, *Gen. Rel. Grav.* **2**, 303 (1971).
- [6] F. S. Coelho, C. Herdeiro, and M. O. P. Sampaio, *JHEP* **1412**, 119 (2014), arXiv:1410.0964 [hep-th].
- [7] F. Pretorius, *Phys. Rev. Lett.* **95**, 121101 (2005), gr-qc/0507014.
- [8] M. Campanelli, C. O. Lousto, P. Marronetti, and Y. Zlochower, *Phys. Rev. Lett.* **96**, 111101 (2006), gr-qc/0511048.
- [9] J. G. Baker, J. Centrella, D.-I. Choi, M. Koppitz, and J. van Meter, *Phys. Rev. Lett.* **96**, 111102 (2006), gr-qc/0511103.
- [10] U. Sperhake, V. Cardoso, F. Pretorius, E. Berti, and J. A. Gonzalez, *Phys. Rev. Lett.* **101**, 161101 (2008), arXiv:0806.1738 [gr-qc].
- [11] U. Sperhake, V. Cardoso, F. Pretorius, E. Berti, T. Hinderer, and N. Yunes, *Phys. Rev. Lett.* **103**, 131102 (2009), arXiv:0907.1252 [gr-qc].
- [12] M. W. Choptuik and F. Pretorius, *Phys. Rev. Lett.* **104**, 111101 (2010), arXiv:0908.1780 [gr-qc].
- [13] W. E. East and F. Pretorius, *Phys. Rev. Lett.* **110**, 101101 (2013), arXiv:1210.0443 [gr-qc].
- [14] L. Rezzolla and K. Takami, *Class. Quant. Grav.* **30**, 012001 (2013), arXiv:1209.6138 [gr-qc].
- [15] U. Sperhake, E. Berti, V. Cardoso, and F. Pretorius, *Phys. Rev. Lett.* **111**, 041101 (2013), arXiv:1211.6114 [gr-qc].

- [16] U. Sperhake, E. Berti, V. Cardoso, and F. Pretorius, Phys. Rev. **D93**, 044012 (2016), arXiv:1511.08209 [gr-qc].
- [17] M. Siino, Int.J.Mod.Phys. **D22**, 1350050 (2013), arXiv:0909.4827 [gr-qc].
- [18] E. Berti, V. Cardoso, T. Hinderer, M. Lemos, F. Pretorius, *et al.*, Phys. Rev. **D81**, 104048 (2010), arXiv:1003.0812 [gr-qc].
- [19] I. Ruchlin, J. Healy, C. O. Lousto, and Y. Zlochower, (2014), arXiv:1410.8607 [gr-qc].
- [20] H. Nakano, J. Healy, C. O. Lousto, and Y. Zlochower, Phys. Rev. **D91**, 104022 (2015), arXiv:1503.00718 [gr-qc].
- [21] M. Alcubierre, Class. Quant. Grav. **20**, 607 (2003), gr-qc/0210050.
- [22] D. Alic, C. Bona-Casas, C. Bona, L. Rezzolla, and C. Palenzuela, Phys. Rev. **D85**, 064040 (2012), arXiv:1106.2254 [gr-qc].
- [23] M. Ansorg, B. Brügmann, and W. Tichy, Phys. Rev. **D70**, 064011 (2004), gr-qc/0404056.
- [24] J. W. York, Phys. Rev. Lett. **82**, 1350 (1999).
- [25] G. B. Cook, Living Rev. Rel. **3**, 5 (2000), arXiv:gr-qc/0007085 [gr-qc].
- [26] H. P. Pfeiffer and J. York, James W., Phys. Rev. D **67**, 044022 (2003), gr-qc/0207095.
- [27] M. Alcubierre, *Introduction to 3+1 Numerical Relativity, by Miguel Alcubierre. ISBN 978-0-19-920567-7 (HB). Published by Oxford University Press, Oxford, UK, 2008.* (Oxford University Press, 2008).
- [28] Y. Zlochower, J. G. Baker, M. Campanelli, and C. O. Lousto, Phys. Rev. **D72**, 024021 (2005), arXiv:gr-qc/0505055.
- [29] T. Nakamura, K. Oohara, and Y. Kojima, Prog. Theor. Phys. Suppl. **90**, 1 (1987).
- [30] M. Shibata and T. Nakamura, Phys. Rev. **D52**, 5428 (1995).
- [31] T. W. Baumgarte and S. L. Shapiro, Phys. Rev. **D59**, 024007 (1998), gr-qc/9810065.
- [32] C. O. Lousto and Y. Zlochower, Phys. Rev. **D77**, 024034 (2008), arXiv:0711.1165 [gr-qc].
- [33] Cactus Computational Toolkit home page: <http://cactuscode.org>.
- [34] Einstein Toolkit home page: <http://einsteintoolkit.org>.
- [35] E. Schnetter, S. H. Hawley, and I. Hawke, Class. Quant. Grav. **21**, 1465 (2004), gr-qc/0310042.
- [36] J. Thornburg, Class. Quant. Grav. **21**, 743 (2004), gr-qc/0306056.
- [37] O. Dreyer, B. Krishnan, D. Shoemaker, and E. Schnetter, Phys. Rev. **D67**, 024018 (2003), gr-qc/0206008.
- [38] J. Winicour, in *General Relativity and Gravitation Vol 2*, edited by A. Held (Plenum, New York, 1980) pp. 71–96.
- [39] M. Campanelli and C. O. Lousto, Phys. Rev. **D59**, 124022 (1999), arXiv:gr-qc/9811019 [gr-qc].
- [40] C. O. Lousto and Y. Zlochower, Phys. Rev. **D76**, 041502(R) (2007), gr-qc/0703061.
- [41] M. Alcubierre, B. Brügmann, P. Diener, M. Koppitz, D. Pollney, E. Seidel, and R. Takahashi, Phys. Rev. **D67**, 084023 (2003), gr-qc/0206072.
- [42] J. R. van Meter, J. G. Baker, M. Koppitz, and D.-I. Choi, Phys. Rev. **D73**, 124011 (2006), gr-qc/0605030.
- [43] G. Cook and J. W. York, Phys. Rev. D **41**, 1077 (1990).
- [44] S. Dain, C. O. Lousto, and R. Takahashi, Phys. Rev. **D65**, 104038 (2002), arXiv:gr-qc/0201062.
- [45] C. O. Lousto, H. Nakano, Y. Zlochower, B. C. Mundim, and M. Campanelli, Phys. Rev. **D85**, 124013 (2012), arXiv:1203.3223 [gr-qc].
- [46] L. Smarr, Phys. Rev. **D15**, 2069 (1977).